AIMS Mathematics

https://www.aimspress.com/journal/Math

AIMS Mathematics, 11(8): 26470–26502.
DOI: 10.3934/math.20261062
Received: 15 May 2026
Revised: 29 July 2026
Accepted: 10 August 2026
Published: 25 August 2026

Research article

Geometric trajectory stabilization and parabolic modal rate matching in impulsive delayed Cohen–Grossberg neural networks

Gülden Altay Suroğlu and Münevver Tuz*

Department of Mathematics, Faculty of Science, Fırat University, Elazığ 23119, Türkiye; galtay@firat.edu.tr

* **Correspondence:** Email: mtuz@firat.edu.tr.

Abstract: This study investigated how exponential stability in impulsive delayed Cohen–Grossberg neural networks is reflected in the geometry of the error trajectory and in an auxiliary reaction–diffusion description. The analysis distinguished rigorous consequences of exponential stability from regular-point and finite-horizon geometric diagnostics. It was shown that exponential convergence of the error norm does not, in general, imply decay of the classical curvature. Instead, a speed-weighted curvature, representing the normal component of the error acceleration, satisfies an exponential upper bound under the stated higher-order regularity assumptions. An auxiliary reaction–diffusion model with multiplicative contractive impulses was then analysed by semigroup and Duhamel estimates, and a periodic Fourier-mode formulation was used to characterize transient rate matching between modal and forcing decay rates. Spectral graph estimates further provided a rigorous exponential envelope for the network disagreement energy. Numerical experiments supported these distinctions: The weighted-curvature diagnostic exhibited a fitted decay rate of 1.0478 with $R^2 = 0.9914$, while 456 of 500 Monte Carlo realizations satisfied the convergence criterion. The near-matching modal response had a peak ratio of 1.2553 relative to the selected detuned case, and the topology experiment detected statistically significant differences in both classical-curvature behavior and finite-horizon accumulated curvature. Overall, the results showed that norm stability rigorously controls weighted geometric and graph-energy quantities, whereas classical curvature and topology-dependent geometric effects should be interpreted as empirical finite-horizon diagnostics.

Keywords: Cohen–Grossberg neural networks; impulsive systems; trajectory geometry; parabolic modal rate matching; spectral graph analysis
Mathematics Subject Classification: 34A37, 34D23, 53A04, 34C27, 92B20

1. Introduction

Recurrent neural networks have long been studied for their role in associative memory and collective information processing. The starting point is Hopfield's model, which framed associative recall as the dynamics of a recurrent system [1]; Kosko later carried this idea over to heteroassociative memory through the bidirectional associative memory (BAM) architecture [2]. Once such models were in place, their stability—especially under transmission delays—became the main object of analysis [3].

The Cohen–Grossberg neural network (CGNN) of Cohen and Grossberg [4] sits above many of these models as a common framework, and much of the subsequent stability theory was worked out for BAM networks carrying periodic, time-varying, or discrete delays [5–7]. The existence and stability of almost periodic solutions for BAM neural networks with delays were investigated in [8]. The same questions were then pushed toward almost-periodic, impulsive, and delayed Cohen–Grossberg-type systems, which are closer to the setting of the present paper [9–12].

Delays are unavoidable in practical neural networks because signal transmission and information processing are not instantaneous; even moderate delays may alter the qualitative dynamics of a network and induce oscillatory instability [13]. This is why so much effort has gone into sharp stability criteria for delayed and impulsive networks [14, 15]. Impulsive effects raise a separate difficulty: They model abrupt jumps in the state caused by switching, discrete control, or synaptic reconfiguration [16–18], and once they act together with delays, the dynamics become markedly harder to control [19].

A further layer of realism is provided by *almost periodic* coefficients and inputs. Almost periodic functions generalize classical periodicity and provide a natural framework for describing recurrent but nonperiodic temporal behavior [20–23]. Within neural-network models, the existence and stability of almost periodic solutions have consequently received considerable attention. Liu, You, and Cao investigated generalized Hopfield neural networks with time-varying delays [24], while Wan et al. established exponential-stability criteria for generalized Cohen–Grossberg neural networks with discrete delays [14]. Xiang et al. studied almost periodic solutions for Cohen–Grossberg-type BAM networks with distributed delays [25], and related developments have incorporated impulsive and stochastic delayed effects [8, 26].

Almost periodic impulsive BAM neural networks with variable delays on time scales were investigated, whereas impulsive inertial neural networks with unpredictable and Poisson-stable oscillations were considered in [19]. These developments provide important foundations for the simultaneous analysis of recurrent temporal structure, delays, and impulsive effects. In particular, the interaction of almost periodic coefficients, time-varying delays, and impulsive perturbations in Cohen–Grossberg neural networks provides the stability-theoretic background for the present geometric investigation [12].

Our companion paper [12] established the existence and global exponential stability of almost periodic solutions for an impulsive Cohen–Grossberg-type BAM neural network with time-varying delays. The analysis was based on a Banach contraction argument, a Lyapunov functional incorporating history terms, and a generalized impulsive Gronwall inequality. In particular, the stability result yields constants $M \geq 1$ and $\mu > 0$ such that

$$\|x(t) - x^*(t)\| \leq Me^{-\mu(t-t_0)}\|x(t_0) - x^*(t_0)\|, \qquad t \geq t_0. \tag{1.1}$$

Although estimate (1.1) provides a quantitative description of convergence in the norm, it does not characterize the geometry of the corresponding error trajectory in state space. This motivates a natural question: *What geometric information can be extracted from the convergent trajectory beyond its norm decay?*

Existing stability studies of delayed, impulsive, and Cohen–Grossberg-type neural networks are predominantly formulated in terms of norm estimates, Lyapunov functionals, matrix inequalities, and related stability criteria [9, 27, 28]. Such approaches provide powerful information about convergence and stability, but they do not directly characterize geometric quantities associated with the error trajectory, such as classical curvature, regular-point torsion, or the normal-acceleration quantity considered in the present work. The purpose of this study is therefore to complement, rather than replace, the norm-based stability framework with a geometric description of the convergent error dynamics.

The present paper addresses this gap by viewing the error trajectory $\gamma_e(t) = x(t) - x^*(t)$ as a curve in state space and by separating quantities that follow rigorously from exponential stability from those that remain regular-point or finite-horizon diagnostics. We address the following four questions.

- Which geometric quantity is genuinely controlled by exponential norm convergence? In particular, why can classical curvature fail to decay even when $\|e(t)\|$ decays exponentially?
- How does a multiplicative impulsive jump act on an auxiliary reaction–diffusion deviation field, and what global H_0^1 bound follows when the continuous forcing decays exponentially?
- What transient response is produced when the decay rate $\rho_m = \nu\xi_m^2 + \lambda^2$ of a periodic partial differential equation (PDE) mode approaches the forcing decay rate μ, and how can a regular-point Frenet wavenumber be used solely as a diagnostic mode-selection device?
- What does the graph Laplacian control rigorously, and which curvature- or topology-related effects should instead be interpreted as empirical finite-horizon observations?

This geometric viewpoint is not typically part of the norm-based neural-network stability framework discussed above, although trajectory-based geometric methods have a well-established role in geometric control theory [29] and classical differential geometry [30, 31]. The dwell-time framework used in the impulsive analysis is related to the classical switched-system approach of [32]. In the present work, the auxiliary parabolic problem is introduced as a deliberately separate reaction–diffusion diagnostic model rather than as a PDE derived from the finite-dimensional CGNN equations. Its periodic modal calculation is used as a controlled rate-matching diagnostic; it is not interpreted as classical oscillator resonance or as an impulse-generated wave mechanism.

Related developments further illustrate the breadth of analytical tools used in delayed and nonlinear dynamical systems. General delay equations and their oscillatory behavior provide part of the broader theoretical background [33, 34], while almost-periodic synchronization and stability have been investigated for delayed neural networks and Cohen–Grossberg-type systems [28, 35, 36]. Discontinuous or impact-type neural dynamics provide another perspective on nonsmooth and impulsive behavior [37, 38]. Beyond neural networks, delayed fractional-order systems also exhibit rich qualitative dynamics [39], illustrating that delay-induced phenomena occur across substantially different classes of nonlinear models. Finally, spectral graph methods provide the mathematical framework for relating network topology to Laplacian quantities [40], whereas delay-dependent collective dynamics in networked multi-agent systems offer a complementary network-level perspective [41].

Main contributions

The paper establishes four results, each addressing a different geometric aspect of the converging trajectory.

(1) **Weighted geometric stabilization** (Theorem 5.1, §5).

Exponential norm convergence does not, in general, imply decay of the classical curvature $\kappa(t)$. The relevant speed-weighted quantity is the weighted curvature

$$\mathcal{K}(t) := \kappa(t) v_e(t)^2, \qquad v_e(t) = \|\dot{e}(t)\|,$$

which is exactly the magnitude of the normal component of the error acceleration:

$$\mathcal{K}(t) = \left\| P_{T(t)^\perp} \ddot{e}(t) \right\|.$$

Under the exponential acceleration estimate in Assumption (A9),

$$\mathcal{K}(t) \le C_a e^{-\mu(t-t_0)} \|e(t_0)\|.$$

This estimate requires no positive lower bound on the speed and therefore does not require a positive lower bound for $v_e(t)$. A logarithmic-spiral counterexample is included to show explicitly why the corresponding statement for $\kappa(t)$ alone is false.

(2) **Impulsively contracted reaction–diffusion response** (Theorem 5.4, §5). The deviation field is modeled on a finite arc-length interval by a damped reaction–diffusion equation with homogeneous Dirichlet boundary conditions. The scalar impulsive operator $J_k = (1 - \delta_k) I$ is contractive and therefore cannot increase the H_0^1 norm. Under an explicit H_0^1 forcing estimate, the solution satisfies a global Duhamel bound. For $\lambda^2 \neq \mu$,

$$\|u(\cdot, t)\|_{H_0^1} \le e^{-\lambda^2 (t-t_0)} \|u_0\|_{H_0^1} + C_F \frac{\left| e^{-\mu(t-t_0)} - e^{-\lambda^2 (t-t_0)} \right|}{|\lambda^2 - \mu|},$$

while the limiting case $\lambda^2 = \mu$ is $C_F (t - t_0) e^{-\mu(t-t_0)}$ for the forced contribution.

(3) **Parabolic modal rate-matching analysis** (Proposition 5.6, §5). On a periodic arc-length domain, each spatial Fourier mode satisfies a scalar dissipative equation with modal decay rate

$$\rho_m = \nu \xi_m^2 + \lambda^2.$$

If the forcing amplitude of that mode decays like $e^{-\mu t}$, then the forced response is governed by the exact difference quotient

$$\frac{e^{-\mu\theta} - e^{-\rho_m \theta}}{\rho_m - \mu}.$$

The apparent singularity at $\rho_m = \mu$ is removable and converges to $\theta e^{-\mu\theta}$, whose peak occurs at $\theta = 1/\mu$. When a geometric diagnostic is desired, the periodic length may be chosen so that a permitted Fourier wavenumber coincides with the selected regular-point Frenet frequency diagnostic $\omega_g(t^*)$.

(4) **Spectral error-energy envelope** (Theorem 6.2, §6). For a symmetric nonnegative synaptic graph, the graph diffusion energy

$$\mathcal{E}(t) = \frac{1}{2} e(t)^{\top} L(t) e(t)$$

satisfies

$$\mathcal{E}(t) \le \frac{\bar{\lambda}_n}{2} M^2 \|e(t_0)\|^2 e^{-2\mu(t-t_0)},$$

where $\bar{\lambda}_n := \sup_{t \ge t_0} \lambda_n(L(t)) < \infty$. Thus the graph spectrum controls a rigorous upper envelope for the spatial disagreement energy. The theorem does *not* imply that the classical curvature, weighted curvature, or Lyapunov exponent is a monotone function of $\lambda_n(L)$.

Paper organization. Section 2 recalls the model and assumptions. Section 3 develops the trajectory geometry. Section 4 introduces the auxiliary reaction–diffusion model. Section 5 proves Theorems 5.1 and 5.4, and Proposition 5.6. Section 6 proves the spectral error-energy envelope. Section 7 presents the numerical experiments, including parameter Monte Carlo and $n = 20$ topology-sensitivity studies. Section 8 concludes the paper.

2. Model and standing assumptions

2.1. The impulsive delayed CGNN

For clarity of the geometric constructions, we work with the single-field formulation below. The two-field BAM model analyzed in [12] motivates the stability setting, but the present single-field system is treated as a reduced model; we do not claim that every result of [12] transfers without additional verification. We consider

$$\dot{x}_i(t) = a_i(x_i(t)) \left[-b_i(x_i(t)) + \sum_{j=1}^{n} w_{ij}(t)\, f_j\big(x_j(t - \tau_{ij}(t))\big) + I_i(t) \right], \quad t \ne t_k, \tag{2.1a}$$

$$x_i(t_k^+) = (1 - \delta_{ik})\, x_i(t_k^-), \quad i = 1, \dots, n, \quad k \in \mathbb{N}, \tag{2.1b}$$

where $a_i > 0$ are amplification functions, $b_i > 0$ are self-regulation functions, $w_{ij}(t)$ are bounded almost periodic synaptic weights, $f_j : \mathbb{R} \to \mathbb{R}$ are Lipschitz activations with $f_j(0) = 0$, $\tau_{ij}(t) \ge 0$ are bounded time-varying delays, $I_i(t)$ are bounded almost periodic inputs, and $\delta_{ik} \in (0, 1)$ are multiplicative impulsive contraction coefficients at impulse times $\{t_k\}$.

2.2. Assumptions (A1)–(A10)

(A1)

$0 < a_i^- \le a_i(u) \le a_i^+ < \infty$ for all $u \in \mathbb{R}$.

(A2)

$|f_j(u) - f_j(v)| \le L_j^f |u - v|$, $f_j(0) = 0$, $L_j^f > 0$.

(A3)

$0 \le \tau_{ij}(t) \le \tau_{\max} < \infty$ uniformly in t.

(A4)
$\delta_{ik} \in (0, 1)$ for all i, k.

(A5)
$\sup_{u\in\mathbb{R}} |f_j(u)| < \infty$. This boundedness is an independent assumption; it does not follow from global Lipschitz continuity alone.

(A6)
$I_i, w_{ij} \in \mathrm{AP}(\mathbb{R}, \mathbb{R})$, bounded by $C_0 > 0$.

(A7)
$a_i, b_i \in \mathrm{AP}(\mathbb{R}, \mathbb{R})$ with $a_i^-, b_i^- > 0$.

(A8)
Dwell-time: $t_{k+1} - t_k \geq H_{\mathrm{imp}} > 0$ for all k.

(A9)
Higher-order regularity and exponential derivative bounds: Between consecutive impulse times, $\gamma_e(t) = e(t) \in C^3$, and there exist $C_a, C_3 > 0$ such that

$$\|\ddot{e}(t)\| \leq C_a e^{-\mu(t-t_0)}\|e(t_0)\|, \qquad \|\dddot{e}(t)\| \leq C_3 e^{-\mu(t-t_0)}\|e(t_0)\|, \qquad t \neq t_k.$$

The acceleration estimate is required by the weighted-curvature theorem; the third-derivative estimate is used only for the three-dimensional torsion diagnostic.

(A10)
Spectral-section graph assumption:

$$W(t) = W(t)^\top, \qquad w_{ij}(t) \geq 0, \qquad w_{ii}(t) = 0.$$

Define

$$D(t) = \mathrm{diag}\left(\sum_j w_{ij}(t)\right), \qquad L(t) = D(t) - W(t).$$

Assume

$$\bar{\lambda}_n = \sup_{t\geq t_0} \lambda_n(L(t)) < \infty.$$

When the lower coercivity estimate is used, also assume

$$\underline{\lambda}_2 = \inf_{t\geq t_0} \lambda_2(L(t)) > 0.$$

2.3. Standing stability hypotheses

The subsequent results require only a bounded reference solution and an exponential error estimate. For the present single-field reduced model, we therefore state these properties explicitly as standing hypotheses. Their two-field BAM analogues are proved in [12]; no direct equivalence between the two models is assumed.

(S1) Reference solution. System (2.1) possesses a bounded reference solution $x^*(t)$ for $t \geq t_0$.

(S2) Global exponential error estimate. There exist constants $M \geq 1$ and $\mu > 0$ such that

$$\|x(t) - x^*(t)\| \leq Me^{-\mu(t-t_0)}\|x(t_0) - x^*(t_0)\|, \qquad t \geq t_0. \tag{2.2}$$

The results below are conditional on (S1)-(S2), together with their stated additional regularity assumptions.

3. Trajectory geometry

3.1. Error trajectory as a curve

Throughout the geometric analysis, we use the error trajectory

$$\gamma_e : [t_0, \infty) \to \mathbb{R}^n, \qquad \gamma_e(t) := e(t) = x(t) - x^*(t).$$

Between consecutive impulse times, the regularity required below is supplied by Assumption (A9), namely, $\gamma_e \in C^3$.

All differential-geometric quantities are evaluated only on the open continuity intervals between impulses. In the common case in which the reference solution is subject to the same multiplicative impulse coefficients as x, the error jump is

$$e_i(t_k^+) = (1 - \delta_{ik})e_i(t_k^-).$$

Define

$$v_e(t) := \|\dot{e}(t)\|, \qquad s_e(t) := \int_{t_0}^{t} v_e(\xi)\, d\xi,$$

where the integral is understood piecewise across impulse times. Jump turning is treated separately in the numerical finite-horizon diagnostic and is not absorbed into the smooth Frenet arc-length.

3.2. Frenet–Serret quantities in three dimensions

The scalar torsion used below is a three-dimensional quantity. Therefore, whenever τ or ω_g is used, we restrict the geometric diagnostic to a three-dimensional error trajectory, as in the baseline numerical experiment. For $n > 3$, a scalar Frenet torsion is not canonical.

At every regular non-inflection point in $\mathbb{R}^3$,

$$v(t) = \|\dot{\gamma}_e e(t)\| > 0, \qquad \dot{\gamma}_e e(t) \times \ddot{\gamma}_e e(t) \neq 0,$$

the Frenet frame is

$$T = \frac{\dot{\gamma}_e}{v_e}, \qquad N = \frac{T'(s)}{\|T'(s)\|}, \qquad B = T \times N. \tag{3.1}$$

The curvature and torsion are

$$\kappa(t) = \frac{\|v_e^2 \ddot{\gamma}_e - \dot{\gamma}_e(\dot{\gamma}_e \cdot \ddot{\gamma}_e)\|}{v_e^4}, \tag{3.2}$$

$$\tau(t) = \frac{\det(\dot{\gamma}_e, \ddot{\gamma}_e, \dddot{\gamma}_e)}{\|\dot{\gamma}_e \times \ddot{\gamma}_e\|^2}. \tag{3.3}$$

Since

$$\kappa(t) = \frac{\|\dot{\gamma}_e \times \ddot{\gamma}_e\|}{v_e(t)^3},$$

we have

$$\|\dot{\gamma}_e \times \ddot{\gamma}_e\|^2 = \kappa(t)^2 v_e(t)^6.$$

Hence

$$\tau(t) = \frac{\det(\dot{\gamma}_e, \ddot{\gamma}_e, \dddot{\gamma}_e)}{\kappa(t)^2 v_e(t)^6}. \tag{3.4}$$

The power v_e^6 is essential; v_e^4 is not equivalent to the standard torsion formula.

Remark 3.1 (On the choice of the Frenet frame)**.** The classical Frenet frame requires regularity of the curve and becomes singular when $v_e(t) = 0$. This is one reason why classical curvature alone is not an appropriate global stability diagnostic for a converging error trajectory. The weighted quantity

$$\mathcal{K}(t) = \kappa(t) v_e(t)^2$$

admits the equivalent acceleration representation

$$\mathcal{K}(t) = \left\| P_{T(t)^\perp} \ddot{e}(t) \right\|$$

at regular points. The weighted-curvature estimate in Theorem 5.1 consequently does not require a positive lower bound on $v_e(t)$.

3.3. Frenet frequency diagnostic

Definition 3.2. For a three-dimensional error trajectory and at a regular non-inflection point where both $\kappa(t)$ and $\tau(t)$ are defined, set

$$\omega_{\mathrm{g}}(t) := \sqrt{\kappa(t)^2 + \tau(t)^2}. \tag{3.5}$$

We call $\omega_{\mathrm{g}}(t)$ the *Frenet frequency diagnostic*.

Both κ and τ have units of inverse arc length, so ω_g has the units of a spatial wavenumber. No stability theorem in this paper asserts that ω_g decays or has a global limit.

Because torsion contains the denominator $\|\dot{e} \times \ddot{e}\|^2$, it is numerically ill-conditioned near inflection points or when velocity and acceleration are nearly parallel. Therefore ω_g is used only on explicitly selected regular samples satisfying a numerical non-degeneracy threshold. It is a diagnostic quantity, not a global stability invariant.

4. Auxiliary reaction–diffusion model

4.1. Scalar frame component and auxiliary field

At a regular three-dimensional point, the error vector may be resolved as

$$e(t) = e_T(t)T(t) + e_N(t)N(t) + e_B(t)B(t).$$

The reaction–diffusion equation below is not asserted to be a three-component PDE exactly equivalent to the CGNN. It is an auxiliary scalar model for one selected frame component or, more generally, for a scalar frame-projected deviation observable. We denote that scalar field by

$$u = u(s,t).$$

If desired, the same estimate can be applied componentwise to separate scalar fields u^T, u^N and u^B. This convention distinguishes the vector error $e(t)$ from the unknown scalar PDE $u(s,t)$.

4.2. Parabolic PDE and impulsive contraction conditions

To match both the functional-analytic setting and the numerical discretization, let the arc-length variable lie on a finite interval

$$\Omega_s := (0,S), \qquad S > 0.$$

We consider the reaction–diffusion problem

$$u_t(s,t) - \nu u_{ss}(s,t) + \lambda^2 u(s,t) = F(s,t), \qquad s \in (0,S), \quad t \in (t_k, t_{k+1}), \tag{4.1a}$$

$$u(0,t) = u(S,t) = 0, \tag{4.1b}$$

$$u(s,t_k^+) = J_k u(s,t_k^-), \qquad J_k = q_k I, \quad 0 \le q_k < 1. \tag{4.1c}$$

Interpretation of the PDE parameters. The coefficients $\nu > 0$ and $\lambda^2 > 0$ are parameters of the auxiliary parabolic model and are not assumed to be explicit functions of the CGNN coefficients a_i, b_i, or w_{ij}. In particular, the diffusion coefficient ν is not derived from the discrete neural coupling of the original CGNN. Rather, it controls spatial smoothing of the auxiliary scalar deviation field along the arc-length coordinate s, whereas λ^2 represents temporal reaction damping. For the mth spatial mode, these two parameters enter through the modal decay rate

$$\rho_m = \nu \xi_m^2 + \lambda^2.$$

Accordingly, ν and λ^2 should be interpreted as parameters of the auxiliary reaction–diffusion model, rather than as intrinsic CGNN parameters. In the numerical modal rate-matching experiment, they are selected to construct controlled near-matching and detuned configurations relative to the empirically estimated CGNN decay rate. This selection is therefore a diagnostic calibration and not a derivation of the PDE coefficients from the CGNN specification.

In the scalar multiplicative-impulse case used numerically, $q_k = 1 - \delta_k$.

The continuous operator

$$A := \nu\partial_{ss} - \lambda^2 I, \qquad D(A) = H^2(0,S) \cap H_0^1(0,S),$$

generates a strongly continuous analytic semigroup on $H_0^1(0,S)$. Because the Dirichlet heat semigroup is contractive and the reaction term contributes the factor $e^{-\lambda^2 t}$,

$$\|e^{At}\phi\|_{H_0^1} \le e^{-\lambda^2 t}\|\phi\|_{H_0^1}, \qquad t \ge 0. \tag{4.2}$$

The impulsive condition (4.1c) is not an additive forcing event. It is a contraction:

$$\|u(\cdot,t_k^+)\|_{H_0^1} = q_k\|u(\cdot,t_k^-)\|_{H_0^1} \le \|u(\cdot,t_k^-)\|_{H_0^1}.$$

Thus impulses can only reduce the norm in the present model. The continuous forcing F is responsible for the inhomogeneous PDE response.

4.3. Motivation and forcing hypothesis

The reaction–diffusion equation is an auxiliary reduced model for a scalar frame-projected deviation; it is not an exact reformulation of the nonlinear delayed CGNN error equation. In particular, (A2) gives

$$|f_j(x_j) - f_j(x_j^*)| \leq L_j^f |x_j - x_j^*|,$$

but does not imply $f_j(x_j) - f_j(x_j^*) = L_j^f(x_j - x_j^*)$. Likewise, a quadratic Taylor remainder cannot be inferred from (A1)–(A8) without additional differentiability assumptions.

The PDE theorem therefore uses the following explicit modeling/regularity hypothesis.

PDE forcing hypothesis (P). For almost every $t \geq t_0$,

$$F(\cdot, t) \in H_0^1(0, S),$$

and there exists $C_F > 0$ such that

$$\|F(\cdot, t)\|_{H_0^1} \leq C_F e^{-\mu(t-t_0)}. \tag{4.3}$$

The separable forcing in the numerical PDE experiment is chosen to satisfy this condition. Thus the CGNN error estimate motivates the temporal scale, while hypothesis (P) supplies the spatial regularity needed for the H_0^1 semigroup bound.

5. Main geometric results

5.1. Weighted geometric stabilization

Theorem 5.1 (Weighted geometric stabilization)**.** *Assume (S1)-(S2) and Assumption* (A9) *hold.*

Let

$$\gamma_e(t) := e(t) = x(t) - x^*(t)$$

be the error trajectory and define

$$v_e(t) := \|\dot{e}(t)\|.$$

At every regular time $t \neq t_k$ for which $v_e(t) > 0$, let $\kappa(t)$ denote the classical curvature of γ_e and define the weighted curvature

$$\mathcal{K}(t) := \kappa(t) v_e(t)^2. \tag{5.1}$$

Then

$$\mathcal{K}(t) \leq C_a e^{-\mu(t-t_0)} \|e(t_0)\|, \qquad t \neq t_k, \tag{5.2}$$

where C_a is the constant in Assumption (A9)*.*

Equivalently, at every regular point,

$$\mathcal{K}(t) = \left\| P_{T(t)^\perp} \ddot{e}(t) \right\|, \qquad T(t) = \frac{\dot{e}(t)}{\|\dot{e}(t)\|}, \tag{5.3}$$

where $P_{T^\perp}$ is the orthogonal projection onto the subspace orthogonal to T.

Thus exponential stability, together with the exponential acceleration estimate in (A9)*, controls the normal acceleration of the error trajectory. No positive lower bound on $v_e(t)$ is required.*

Proof. Fix a regular time $t \neq t_k$ with $v_e(t) > 0$. For the parametrized curve $\gamma_e(t) = e(t)$, the classical curvature is

$$\kappa(t) = \frac{\left\| v_e(t)^2 \ddot{e}(t) - \dot{e}(t) \langle \dot{e}(t), \ddot{e}(t) \rangle \right\|}{v_e(t)^4}. \tag{5.4}$$

Set

$$T(t) := \frac{\dot{e}(t)}{v_e(t)}.$$

Since $\dot{e}(t) = v_e(t) T(t)$,

$$\langle \dot{e}(t), \ddot{e}(t) \rangle = v_e(t) \langle T(t), \ddot{e}(t) \rangle.$$

Therefore

$$\begin{aligned} &v_e(t)^2 \ddot{e}(t) - \dot{e}(t) \langle \dot{e}(t), \ddot{e}(t) \rangle \\ &\qquad = v_e(t)^2 \left[\ddot{e}(t) - \langle T(t), \ddot{e}(t) \rangle T(t) \right]. \end{aligned} \tag{5.5}$$

Substituting (5.5) into (5.4) yields the exact identity

$$\kappa(t) v_e(t)^2 = \| \ddot{e}(t) - \langle T(t), \ddot{e}(t) \rangle T(t) \| . \tag{5.6}$$

The vector on the right-hand side is the orthogonal projection of $\ddot{e}(t)$ onto $T(t)^{\perp}$. Hence

$$\mathcal{K}(t) = \left\| P_{T(t)^{\perp}} \ddot{e}(t) \right\| .$$

Because an orthogonal projection is norm non-increasing,

$$\mathcal{K}(t) \leq \| \ddot{e}(t) \|.$$

Assumption (A9) gives

$$\| \ddot{e}(t) \| \leq C_a e^{-\mu(t-t_0)} \| e(t_0) \|.$$

Combining the last two inequalities proves (5.2).

The proof contains no division by a positive lower bound for $v_e(t)$. Accordingly, the estimate does not acquire a factor of the form $v_{\min}(T)^{-2}$ as the trajectory slows down. □

Remark 5.2 (Why classical curvature need not decay)**.** Exponential convergence of a trajectory does not by itself imply decay of its classical curvature. Consider

$$e(t) = r_0 e^{-t} (\cos t, \sin t), \qquad r_0 > 0.$$

Then

$$\| e(t) \| = r_0 e^{-t} \longrightarrow 0, \qquad v_e(t) = \sqrt{2}\, r_0 e^{-t},$$

whereas direct calculation gives

$$\kappa(t) = \frac{e^t}{\sqrt{2}\, r_0} \longrightarrow \infty.$$

Thus even an exponentially convergent trajectory may have increasing classical curvature as its speed tends to zero.

In contrast,

$$\mathcal{K}(t) = \kappa(t) v_e(t)^2 = \sqrt{2}\, r_0 e^{-t} \longrightarrow 0.$$

The weighted curvature therefore captures the dynamically relevant normal acceleration, while $\kappa(t)$ alone is not a generally valid measure of stabilization.

Remark 5.3. The quantity $\mathcal{K}(t) = \kappa(t)v_e(t)^2$ should not be described as a parameterization-invariant curvature invariant. It is a speed-weighted geometric diagnostic with the direct dynamical interpretation

$$\mathcal{K}(t) = \|a_\perp(t)\|,$$

where $a_\perp$ is the normal component of the error acceleration. This interpretation is exactly what removes the singular factor v_e^{-2} that appears when classical curvature is considered in isolation.

5.2. Impulsively contracted reaction–diffusion response

Theorem 5.4 (Impulsively contracted reaction–diffusion response)**.** *Let u satisfy* (4.1) *on* $(0, S)$*, assume $u_0 := u(\cdot, t_0) \in H_0^1(0, S)$, and suppose the PDE forcing hypothesis* (P) *holds. Assume also that*

$$0 \le q_k \le 1$$

for every impulse.

Then, for all $t \ge t_0$,

$$\|u(\cdot, t)\|_{H_0^1} \le e^{-\lambda^2(t-t_0)}\|u_0\|_{H_0^1} + C_F\,\Psi_{\lambda^2,\mu}(t - t_0), \tag{5.7}$$

where

$$\Psi_{\lambda^2,\mu}(\theta) := \begin{cases} \dfrac{\left|e^{-\mu\theta} - e^{-\lambda^2\theta}\right|}{|\lambda^2 - \mu|}, & \lambda^2 \ne \mu, \\ \theta e^{-\mu\theta}, & \lambda^2 = \mu, \end{cases} \qquad \theta \ge 0. \tag{5.8}$$

In particular,

$$\|u(\cdot, t)\|_{H_0^1} \longrightarrow 0 \qquad (t \to \infty).$$

The impulsive multipliers do not enlarge this upper bound; they can only decrease the norm relative to the corresponding continuously forced problem without jumps.

Proof. Let

$$S_A(t) := e^{At}, \qquad A = \nu\partial_{ss} - \lambda^2 I$$

on $H_0^1(0, S)$. By (4.2),

$$\|S_A(t)\|_{\mathcal{L}(H_0^1)} \le e^{-\lambda^2 t}.$$

For $t \ge s$, let $U(t, s)$ denote the evolution operator obtained by alternating the continuous semigroup with the scalar jump operators $J_k = q_k I$ occurring between s and t. Since J_k commutes with S_A and $\|J_k\| = q_k \le 1$,

$$U(t, s) = \left(\prod_{s<t_k\le t} q_k\right) S_A(t - s),$$

and consequently,

$$\|U(t, s)\|_{\mathcal{L}(H_0^1)} \le e^{-\lambda^2(t-s)}. \tag{5.9}$$

The variation-of-constants formula for the impulsive problem is

$$u(\cdot, t) = U(t, t_0)u_0 + \int_{t_0}^{t} U(t, \sigma)F(\cdot, \sigma)\, d\sigma. \tag{5.10}$$

Using (5.9) and hypothesis (P),

$$\|u(\cdot,t)\|_{H_0^1} \le e^{-\lambda^2(t-t_0)}\|u_0\|_{H_0^1} + C_F \int_{t_0}^{t} e^{-\lambda^2(t-\sigma)} e^{-\mu(\sigma-t_0)}\, d\sigma. \tag{5.11}$$

Set $\theta = t - t_0$ and $r = \sigma - t_0$. The convolution becomes

$$\int_0^\theta e^{-\lambda^2(\theta-r)} e^{-\mu r}\, dr.$$

If $\lambda^2 \neq \mu$, direct integration yields

$$\frac{e^{-\mu\theta} - e^{-\lambda^2\theta}}{\lambda^2 - \mu}.$$

This quantity is nonnegative, and its absolute-value representation is the first branch of (5.8). If $\lambda^2 = \mu$, the integral is exactly

$$\theta e^{-\mu\theta}.$$

Substitution into (5.11) proves (5.7).

Both branches of $\Psi_{\lambda^2,\mu}(\theta)$ tend to zero as $\theta \to \infty$, so the solution norm tends to zero. Finally, the factor

$$\prod_{s<t_k\le t} q_k$$

never exceeds one, proving that the multiplicative impulses are contracting rather than amplifying in this model. □

Remark 5.5. Theorem 5.4 deliberately avoids the earlier terminology "impulse-induced wave packet". With the jump law $u(t_k^+) = q_k u(t_k^-)$ and $0 \le q_k < 1$, an impulse removes amplitude; it does not inject it. A genuinely impulse-generated PDE wave would require an additive jump, such as

$$u(t_k^+) = u(t_k^-) + g_k,$$

or a distributional forcing term concentrated at t_k. Neither is assumed in the present model.

5.3. *Parabolic modal rate matching*

The reaction–diffusion equation is dissipative and first order in time, so the phenomenon considered here is not resonance in the classical undamped-oscillator sense. It is a *rate-matching transient*: The decay rate of a forced spatial mode approaches the exponential decay rate of its forcing. This produces the limiting factor $\theta e^{-\mu\theta}$ but no singular blow-up.

For the modal calculation, we use a periodic arc-length domain $\mathbb{T}_S = \mathbb{R}/S\mathbb{Z}$. This is the setting used in the numerical rate-matching experiment. It is distinct from the homogeneous Dirichlet setting of Theorem 5.4, but the same reaction–diffusion operator and Duhamel calculation apply.

Proposition 5.6 (Parabolic modal rate matching)**.** *Consider*

$$u_t - \nu u_{ss} + \lambda^2 u = F$$

on the periodic domain $\mathbb{T}_S$ between two consecutive impulse times. Let

$$\xi_m := \frac{2\pi m}{S}, \qquad m \in \mathbb{Z},$$

and denote by $\widehat{u}_m(t)$ and $\widehat{F}_m(t)$ the corresponding Fourier coefficients. Fix t^* strictly between two impulses and put

$$\theta := t - t^*, \qquad \rho_m := \nu\xi_m^2 + \lambda^2 > 0.$$

Assume that, on the same inter-impulse interval $t \in [t^*, t_{k^*+1})$,

$$|\widehat{F}_m(t)| \leq B_m e^{-\mu(t-t^*)}, \qquad t \in [t^*, t_{k^*+1}), \tag{5.12}$$

for some $B_m \geq 0$.

Then the forced component of the mth mode satisfies, for $\rho_m \neq \mu$,

$$|\widehat{u}_{m,p}(t)| \leq B_m \frac{|e^{-\mu\theta} - e^{-\rho_m\theta}|}{|\rho_m - \mu|}, \tag{5.13}$$

whereas for $\rho_m = \mu$,

$$|\widehat{u}_{m,p}(t)| \leq B_m \theta e^{-\mu\theta}. \tag{5.14}$$

Moreover,

$$\lim_{\rho_m \to \mu} \frac{e^{-\mu\theta} - e^{-\rho_m\theta}}{\rho_m - \mu} = \theta e^{-\mu\theta}, \tag{5.15}$$

so the apparent singularity is removable. On the unrestricted half-line $\theta \geq 0$, the limiting envelope reaches its maximum at

$$\theta = \frac{1}{\mu}, \tag{5.16}$$

with peak value

$$\frac{B_m}{e\mu}. \tag{5.17}$$

For the actual inter-impulse problem, this peak is attained only if

$$\frac{1}{\mu} < t_{k^*+1} - t^*.$$

If the next impulse occurs earlier, the limiting envelope is increasing throughout the available interval and its maximum on that interval is attained at $t = t_{k^*+1}^-$.

For $\rho_m \neq \mu$, the exact maximum of the normalized kernel on the unrestricted half-line $\theta \geq 0$,

$$G_{\rho_m,\mu}(\theta) := \frac{|e^{-\mu\theta} - e^{-\rho_m\theta}|}{|\rho_m - \mu|},$$

occurs at

$$\theta_m^* = \frac{\log(\rho_m/\mu)}{\rho_m - \mu} \tag{5.18}$$

and

$$\theta_m^* \longrightarrow \frac{1}{\mu} \qquad \text{as } \rho_m \to \mu.$$

No divergence of either unrestricted peak time or peak amplitude occurs as the two rates approach one another. On a finite inter-impulse interval, the observed maximum is instead taken over $0 \leq \theta < t_{k^*+1} - t^*$.

Proof. Taking the periodic Fourier coefficient of the PDE at wavenumber ξ_m gives

$$\frac{d}{dt}\widehat{u}_m(t) + \rho_m\widehat{u}_m(t) = \widehat{F}_m(t), \qquad \rho_m = \nu\xi_m^2 + \lambda^2. \tag{5.19}$$

For $t \in [t^*, t_{k^*+1})$, the forced component with zero modal initial data at t^* is

$$\widehat{u}_{m,p}(t) = \int_{t^*}^{t} e^{-\rho_m(t-\sigma)}\widehat{F}_m(\sigma)\,d\sigma.$$

Using (5.12),

$$|\widehat{u}_{m,p}(t)| \le B_m \int_{t^*}^{t} e^{-\rho_m(t-\sigma)}e^{-\mu(\sigma-t^*)}\,d\sigma.$$

With $r = \sigma - t^*$ and $\theta = t - t^*$, this becomes

$$B_m \int_0^{\theta} e^{-\rho_m(\theta-r)}e^{-\mu r}\,dr.$$

If $\rho_m \neq \mu$, direct integration gives

$$B_m \frac{e^{-\mu\theta} - e^{-\rho_m\theta}}{\rho_m - \mu},$$

whose value is nonnegative; taking absolute values yields (5.13). If $\rho_m = \mu$, the integral is exactly

$$B_m\theta e^{-\mu\theta},$$

which proves (5.14).

For fixed θ, the mean value theorem applied to $r \mapsto e^{-r\theta}$ gives

$$\frac{e^{-\mu\theta} - e^{-\rho_m\theta}}{\rho_m - \mu} = \theta e^{-\widetilde{\rho}\theta}$$

for some $\widetilde{\rho}$ between μ and ρ_m. Letting $\rho_m \to \mu$ proves (5.15).

The function

$$g(\theta) = \theta e^{-\mu\theta}$$

has the derivative

$$g'(\theta) = e^{-\mu\theta}(1 - \mu\theta),$$

so its unique positive maximum occurs at $\theta = 1/\mu$ and equals $1/(e\mu)$. This gives (5.16) and (5.17). For the inter-impulse problem, this critical point belongs to the admissible time interval only when $1/\mu < t_{k^*+1} - t^*$. Otherwise g is still increasing on the available interval and the supremum is reached as $t \uparrow t_{k^*+1}$.

Finally, for $\rho_m \neq \mu$, differentiating $e^{-\mu\theta} - e^{-\rho_m\theta}$ and solving the nonzero critical-point equation gives

$$\rho_m e^{-\rho_m\theta} = \mu e^{-\mu\theta},$$

hence

$$\theta_m^* = \frac{\log(\rho_m/\mu)}{\rho_m - \mu}.$$

L'Hôpital's rule gives $\theta_m^* \to 1/\mu$ as $\rho_m \to \mu$. □

Remark 5.7 (Connection with the trajectory geometry)**.** The modal proposition is valid for every permitted periodic wavenumber ξ_m and does not require a geometric interpretation. To connect it with the trajectory geometry at a regular time t^*, one may select a mode whose wavenumber is close to

$$\omega_g(t^*) = \sqrt{\kappa(t^*)^2 + \tau(t^*)^2}.$$

For a pointwise diagnostic, one may choose

$$S = \frac{2\pi}{\omega_g(t^*)},$$

so that $\xi_1 = \omega_g(t^*)$. In the numerical experiment, however, we use the median value $\bar{\omega}_g$ over a prescribed regular sampling window and set $S = 2\pi/\bar{\omega}_g$. Both constructions are deliberate diagnostic choices, not theorems asserting that a Frenet frequency is an eigenfrequency of a fixed physical domain.

Remark 5.8 (Terminology)**.** Because Eq (5.19) is a first-order dissipative equation, "rate matching" or "rate-matching transient" is more precise than classical resonance. In particular, the limit $\rho_m \to \mu$ is finite. The analysis predicts an enhanced or prolonged transient relative to selected detuned cases, not an unbounded response.

6. Spectral error-energy bounds

The weighted-curvature result of Section 5 is a statement about the normal acceleration of the error trajectory. It does not, by itself, provide a monotone relation between trajectory curvature and the graph spectrum. We therefore separate the two questions. In this section, we derive only those consequences of the synaptic Laplacian that follow rigorously from the norm-stability estimate.

6.1. Synaptic Laplacian and graph diffusion energy

Under Assumption (A10), define

$$L(t) := D(t) - W(t), \qquad D(t) := \operatorname{diag}\left(\sum_j w_{ij}(t)\right). \tag{6.1}$$

For every t, $L(t)$ is symmetric positive semidefinite and therefore has real eigenvalues

$$0 = \lambda_1(L(t)) \le \lambda_2(L(t)) \le \cdots \le \lambda_n(L(t)).$$

For a connected nonnegative graph, $\ker L(t) = \operatorname{span}\{\mathbf{1}\}$.

Definition 6.1 (Network diffusion energy)**.** The *network diffusion energy* of the error is

$$\mathcal{E}(t) := \frac{1}{2} e(t)^\top L(t) e(t). \tag{6.2}$$

For nonnegative symmetric weights,

$$\mathcal{E}(t) = \frac{1}{4} \sum_{i,j} w_{ij}(t)\big(e_i(t) - e_j(t)\big)^2 \ge 0. \tag{6.3}$$

Thus $\mathcal{E}(t)$ measures instantaneous graph disagreement of the error rather than the total error magnitude.

6.2. Main spectral estimate

Theorem 6.2 (Spectral error-energy envelope)**.** *Assume (S1)-(S2) and Assumption* (A10) *hold. Let*

$$\bar{\lambda}_n := \sup_{t \geq t_0} \lambda_n(L(t)) < \infty.$$

Then, for every $t \geq t_0$,

$$0 \leq \mathcal{E}(t) \leq \frac{\bar{\lambda}_n}{2} M^2 \|e(t_0)\|^2 e^{-2\mu(t-t_0)}. \tag{6.4}$$

Consequently, the graph disagreement energy converges to zero and is dominated by an exponential envelope with exponent 2μ.

If, in addition,

$$\underline{\lambda}_2 := \inf_{t \geq t_0} \lambda_2(L(t)) > 0,$$

then

$$\frac{\underline{\lambda}_2}{2} \|e_\perp(t)\|^2 \leq \mathcal{E}(t) \leq \frac{\bar{\lambda}_n}{2} \|e(t)\|^2, \tag{6.5}$$

where

$$e_\perp(t) := e(t) - \frac{\mathbf{1}^\top e(t)}{n} \mathbf{1}$$

is the component orthogonal to the consensus subspace.

Proof. Because $L(t)$ is symmetric positive semidefinite, the Rayleigh quotient gives

$$0 \leq e(t)^\top L(t) e(t) \leq \lambda_n(L(t)) \|e(t)\|^2.$$

Hence

$$0 \leq \mathcal{E}(t) \leq \frac{\lambda_n(L(t))}{2} \|e(t)\|^2 \leq \frac{\bar{\lambda}_n}{2} \|e(t)\|^2.$$

By (2.2),

$$\|e(t)\| \leq M e^{-\mu(t-t_0)} \|e(t_0)\|.$$

Squaring and substituting yields

$$\mathcal{E}(t) \leq \frac{\bar{\lambda}_n}{2} M^2 \|e(t_0)\|^2 e^{-2\mu(t-t_0)},$$

which proves (6.4).

For the lower estimate, assume $\underline{\lambda}_2 > 0$. For a connected nonnegative graph, $\ker L(t) = \operatorname{span}\{\mathbf{1}\}$. Since $L(t)\mathbf{1} = 0$, only the component $e_\perp(t)$ contributes:

$$e(t)^\top L(t) e(t) = e_\perp(t)^\top L(t) e_\perp(t).$$

The lower Rayleigh inequality therefore gives

$$e_\perp(t)^\top L(t) e_\perp(t) \geq \lambda_2(L(t)) \|e_\perp(t)\|^2 \geq \underline{\lambda}_2 \|e_\perp(t)\|^2.$$

Dividing by two proves the left-hand side of (6.5); the right-hand side follows from the upper Rayleigh estimate. □

6.3. *Interpretation and limitations*

Remark 6.3 (Meaning of the exponent 2μ)**.** Equation (6.4) is an *upper-envelope estimate*. It shows that $\mathcal{E}(t)$ cannot exceed a quantity proportional to $e^{-2\mu(t-t_0)}$. It does not assert that the measured diffusion energy has an exact fitted decay exponent equal to 2μ, nor does it assert monotonicity of $\mathcal{E}(t)$ at every instant when $L(t)$ is time dependent.

Remark 6.4 (What the Laplacian spectrum does and does not control)**.** The largest Laplacian eigenvalue enters the rigorous estimate through the prefactor $\bar{\lambda}_n/2$. The algebraic connectivity enters the coercivity estimate through $\underline{\lambda}_2/2$. These statements concern graph disagreement energy.

No conclusion of the form

$$\kappa(t) \propto \lambda_n(L), \qquad \mathcal{K}(t) \propto \lambda_n(L),$$

or monotonic dependence of either geometric quantity on $\lambda_n(L)$ follows from Theorem 6.2. Likewise, the theorem does not imply that the Lyapunov exponent μ is independent of network architecture: For a family of different networks, the stability constants M and μ may themselves change because the underlying coefficient and coupling conditions change.

Remark 6.5 (Separation from the modal rate-matching criterion)**.** The spectral estimate above and Proposition 5.6 address different mechanisms. The former controls the instantaneous graph disagreement energy through the Laplacian spectrum; the latter controls a forced PDE Fourier mode through the detuning quantity

$$|\nu\omega_g(t^*)^2 + \lambda^2 - \mu|.$$

They may be used jointly as complementary diagnostics, but the present analysis does not yield a single rigorous "unified design rule" combining $\lambda_n(L)$ with the curvature or with the Lyapunov exponent.

Table 1 summarizes the quantities that remain theoretically justified.

Table 1. Spectral and geometric quantities used in the present framework.

Quantity	Meaning	Rigorous role in this paper
μ	Lyapunov envelope exponent	norm-error envelope for a fixed network
$\mathcal{K}(t)$	$\kappa(t)v_e(t)^2$	normal-acceleration magnitude
$\mathcal{E}(t)$	$\frac{1}{2}e^\top L(t)e$	graph disagreement energy
$\bar{\lambda}_n$	$\sup_t \lambda_n(L(t))$	upper prefactor for $\mathcal{E}(t)$
$\underline{\lambda}_2$	$\inf_t \lambda_2(L(t))$	coercivity of disagreement energy
$\omega_g(t)$	$\sqrt{\kappa^2+\tau^2}$	modal wavenumber used in rate-matching analysis
λ^2	PDE reaction parameter	contributes to modal decay/detuning

7. Numerical simulations

7.1. *Baseline parameter set*

Simulation setup. In all deterministic CGNN experiments, we use the activation function

$$f_i(u) = \tanh(u), \qquad i = 1, 2, 3,$$

and the external inputs

$$I_i(t) = 0.05\sin(0.30t).$$

The baseline amplification and self-regulation coefficients are

$$a_i = 1, \qquad b_i = 0.8,$$

respectively. The delay is

$$\tau_{\text{delay}} = 0.25,$$

the impulsive contraction coefficient is

$$\delta = 0.20,$$

and impulses occur every

$$H_{\text{imp}} = 5$$

time units. The delayed system is integrated using MATLAB's `dde23` solver with relative and absolute tolerances 10^{-7} and 10^{-9}, respectively.

The delayed CGNN simulations use MATLAB R2024a with `dde23` and piecewise integration across impulse times; the PDE experiments use the discretizations described in Experiments 2 and 3. Curvature and, at regular three-dimensional samples, torsion are computed from finite-difference derivatives of the numerical error trajectory. The torsion diagnostic uses

$$\tau = \frac{\det(\dot{e}, \ddot{e}, \dddot{e})}{\|\dot{e} \times \ddot{e}\|^2}.$$

The numerical study comprises six experiments: four deterministic diagnostics (Experiments 1–4), a parameter Monte Carlo robustness study (Experiment 5), and a separate $n = 20$ topology-sensitivity study (Experiment 6). The baseline parameters and the experiment-specific modifications are summarized in Table 2. In particular, the table distinguishes the common CGNN parameter set from the separate PDE settings used in Experiments 2 and 3, the coupling-weight sweep performed in Experiment 4, and the parameter ranges employed in the Monte Carlo study.

Table 2. Baseline and experiment-specific parameters. The CGNN baseline has $n = 3$; Experiment 3 is a separate periodic PDE diagnostic without impulsive jumps and Experiment 4 scales only the baseline coupling weights.

Parameter	Baseline / Exp. 1	Exp. 2	Exp. 3	Exp. 4	MC range
n	3	3	3	3	3
a_i	1.0	1.0	1.0	1.0	$[0.7, 1.3]$
b_i	0.8	0.8	0.8	0.8	$[0.5, 1.2]$
$\max \lvert w_{ij} \rvert$	0.15	0.15	0.15	0.02–0.30	$[0.05, 0.30]$
τ_{delay}	0.25	0.25	0.25	0.25	$[0.10, 0.60]$
δ	0.20	0.20	—[a]	0.20	$[0.05, 0.45]$
H_{imp}	5.0	5.0	—[a]	5.0	$[2.0, 8.0]$
λ^2	—	2.00	0.388648 / 0.658648[b]	—	—
ν	—	0.20	2.32×10^{-4}[c]	—	—
S	—	12	0.269249[d]	—	—
$\lambda_n(L)$	0.45	0.45	—[e]	0.06–0.90	—
T	50	50	15[f]	50	50

[a] Experiment 3 is run without impulsive jumps. [b] Near-matching and detuned reaction parameters, respectively. [c] The computation gives $\nu_{\text{res}} \approx 2.32 \times 10^{-4}$ from $\nu_{\text{res}} = 0.25\widehat{\mu}_e/\bar{\omega}_g^2$. [d] $S_{\text{res}} = 2\pi/\bar{\omega}_g$ with $\bar{\omega}_g = 23.335979$. [e] Experiment 3 is a periodic PDE modal diagnostic rather than a graph-Laplacian sweep. [f] The modal PDE is simulated on its dedicated rate-matching diagnostic time grid rather than the $[0, 50]$ CGNN horizon.

7.2. *Experiment 1: weighted geometric stabilization*

The deterministic baseline experiment separates norm convergence from classical-curvature behavior. An exponential fit to the error norm gives

$$\widehat{\mu}_e = 0.5049, \qquad R^2 = 0.9998,$$

confirming clean exponential convergence of the two simulated trajectories. By contrast, fitting the classical curvature to a single exponential over the selected fitting region gives

$$\widehat{\mu}_\kappa = 0.0189, \qquad R^2 = 0.0372.$$

The very small coefficient of determination shows that a classical curvature-decay model is not supported by this trajectory. This is consistent with Remark 5.2: Exponential norm convergence alone does not imply decay of $\kappa(t)$.

Figure 1 illustrates this distinction directly: the error norm exhibits clean exponential convergence, whereas the classical curvature shows substantially more complicated finite-horizon behavior.

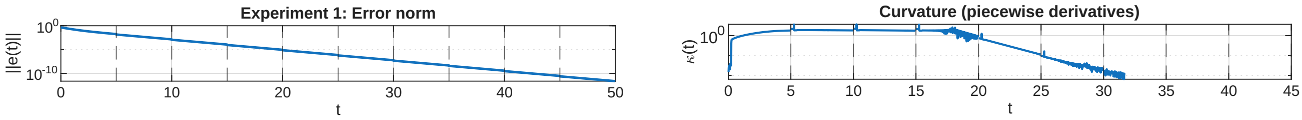

(a) Error norm $\|e(t)\|$ for the baseline CGNN simulation.

(b) Classical curvature $\kappa(t)$ computed using piecewise derivatives between impulsive events.

Figure 1. Geometric diagnostics for Experiment 1. Panel (a) shows the clean exponential convergence of the error norm, whereas panel (b) illustrates that the classical curvature does not exhibit a comparable single-exponential decay. This distinction is consistent with Theorem 5.1 and Remark 5.2.

We therefore evaluate the weighted-curvature diagnostic

$$\mathcal{K}(t) = \kappa(t)v_e(t)^2.$$

Its fitted exponential rate is

$$\widehat{\mu}_{\mathcal{K}} = 1.0478, \qquad R^2 = 0.9914,$$

showing a strong exponential decrease of the normal-acceleration magnitude in the baseline simulation. This numerical result illustrates the quantity controlled by Theorem 5.1; it is not used to claim that the fitted exponent must equal the Lyapunov exponent. For descriptive geometric purposes only, the continuous accumulated curvature on $[0, 50]$ is

$$\Sigma_{\mathrm{cont}} = \int_0^{50} \kappa(t)v_e(t)\,dt \approx 1.331526.$$

The jump-turning contribution is approximately 0.464386, giving the piecewise total-turning diagnostic

$$\Sigma_{\mathrm{piecewise}} \approx 1.795912.$$

These are finite-horizon numerical observables; no global finite-total-curvature theorem is inferred from them. A grid-refinement check gives

Δt	0.020	0.010	0.005
Σ_{cont}	1.331952	1.331526	1.331316

and the last two values differ by only approximately 0.02%. Hence the reported finite-horizon accumulated-curvature diagnostic is numerically well-resolved for the present discretization.

7.3. Experiment 2: reaction–diffusion response

The numerical PDE experiment solves the reaction–diffusion equation on the finite interval $[0, 12]$ with homogeneous Dirichlet boundary conditions, using backward Euler in time and second-order finite differences in space. The impulsive update multiplies the discrete field by $1-\delta$ and therefore acts as a contraction, consistent with Theorem 5.4.

The discrete Duhamel comparator and the numerical H^1 norm give

$$\min_t \frac{B_{\mathrm{disc}}(t)}{\max(\|u(\cdot, t)\|_{H^1}, 10^{-12})} = 0.4612,$$

while the maximum absolute excess of the numerical norm over the comparator is only

$$7.542 \times 10^{-5}.$$

The median relative excess of the comparator is approximately 1.07%.

The small absolute discrepancy may arise from spatial/time discretization and from the discrete comparator construction; without a dedicated PDE mesh-refinement study, its source cannot be identified uniquely. Nevertheless, the ratio 0.4612 shows that the discrete comparator should not be described as a verified pointwise upper bound at every grid time, particularly when the solution norm is extremely small. Accordingly, the present experiment is reported as a numerical consistency check rather than as a proof of the continuous inequality (5.7). The rigorous bound is supplied by Theorem 5.4; a separate mesh-refinement study for the PDE would be required for a strict numerical bound-verification claim.

7.4. Experiment 3: parabolic modal rate matching

The numerical computation evaluates the three-dimensional torsion directly from

$$\tau(t) = \frac{\det(\dot{e}, \ddot{e}, \dddot{e})}{\|\dot{e} \times \ddot{e}\|^2}$$

and retains only numerically regular samples in the prescribed window $5.2 < t < 9.5$. There are 280 valid torsion samples in this window. The representative Frenet frequency diagnostic is the median

$$\bar{\omega}_g = 23.335979.$$

Figure 2 shows the corresponding torsion-numerator diagnostic. Consistent with Section 3.3, it is not interpreted as a global stability quantity and is used only after regularity filtering.

The empirical error-norm decay rate used in the modal diagnostic is

$$\widehat{\mu}_e = 0.504864.$$

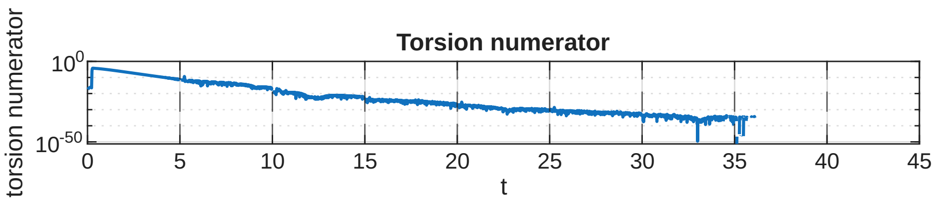

Figure 2. The numerically computed torsion numerator along the baseline three-dimensional error trajectory. The quantity is used only as a regular-point diagnostic; samples entering the Frenet-frequency calculation are restricted by the numerical non-degeneracy criterion described in Section 3.3.

The diffusion coefficient is selected adaptively by

$$\nu_{\text{res}} = \min\left\{0.10, \frac{0.25\,\widehat{\mu}_e}{\bar{\omega}_g^2}\right\}, \tag{7.1}$$

which gives approximately

$$\nu_{\mathrm{res}} = 2.32 \times 10^{-4}.$$

For the present data, the second branch of (7.1) is active, so

$$\nu_{\mathrm{res}}\bar{\omega}_g^2 = 0.25\widehat{\mu}_e.$$

This identity shows that changes in the computed value of $\bar{\omega}_g$ modify ν_{res} while leaving the prescribed modal reaction parameters below unchanged.

For the near-matching case, we prescribe

$$\rho_{\mathrm{near}} = \widehat{\mu}_e + 0.01 = 0.514864,$$

and for the detuned case,

$$\rho_{\mathrm{det}} = \widehat{\mu}_e + 0.28 = 0.784864.$$

Since

$$\rho = \nu_{\mathrm{res}}\bar{\omega}_g^2 + \lambda^2,$$

the corresponding reaction parameters are

$$\lambda_{\mathrm{near}}^2 = 0.388648, \qquad \lambda_{\mathrm{det}}^2 = 0.658648.$$

The analytical modal-response diagnostic gives

$$A_{\mathrm{near}}^{\mathrm{ana}} = 0.721537, \qquad A_{\mathrm{det}}^{\mathrm{ana}} = 0.575041.$$

For the numerical test, the periodic interval is chosen as

$$S_{\mathrm{res}} = \frac{2\pi}{\bar{\omega}_g},$$

so that the fundamental periodic Fourier mode satisfies

$$\xi_1 = \bar{\omega}_g.$$

The numerical PDE experiment is run without impulsive jumps and yields

$$A_{\mathrm{near}}^{\mathrm{num}} = 0.718817, \qquad A_{\mathrm{det}}^{\mathrm{num}} = 0.572645.$$

Hence

$$\frac{A_{\mathrm{near}}^{\mathrm{num}}}{A_{\mathrm{det}}^{\mathrm{num}}} = 1.2553,$$

so the selected near-matching configuration has a peak approximately 25.5% larger than the selected detuned configuration.

As shown in Figure 3, the selected near-matching configuration produces a larger transient response than the selected detuned configuration. This observation is a numerical diagnostic and is not interpreted as a general lower-bound or resonance theorem. The numerical near-matching peak occurs at

$$\theta_{\mathrm{peak}}^{\mathrm{num}} = 1.9600.$$

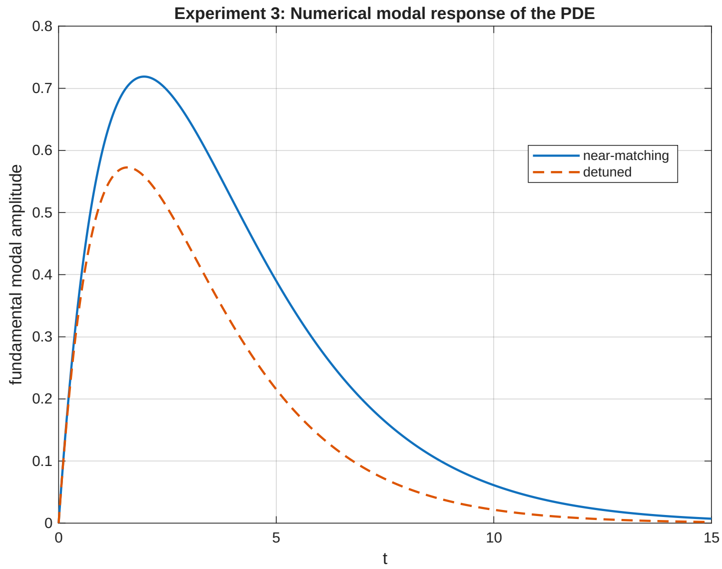

Figure 3. Numerical modal responses for the near-matching and detuned configurations in Experiment 3. The selected near-matching configuration exhibits a larger transient peak than the selected detuned configuration.

The limiting rate-matching characteristic time predicted by Proposition 5.6 is

$$\frac{1}{\widehat{\mu}_e} = 1.9807.$$

The relative difference is approximately 1.0%.

The standard torsion formula yields the representative geometric wavenumber reported above. The near/detuned modal comparison remains unchanged in this experiment because ν_{res} is selected adaptively so that $\nu_{\mathrm{res}}\bar{\omega}_g^2 = 0.25\widehat{\mu}_e$. These results are a consistency check for the modal rate-matching formula; they are not a claim that rate matching globally maximizes the response over all forcings or parameter choices.

7.5. *Experiment 4: spectral scaling diagnostic*

We scale the baseline weight matrix over the prescribed spectral range and compute the classical-curvature diagnostic

$$\widehat{C}_\kappa := \max_t\{\kappa(t)e^{\widehat{\mu}_e t}\}.$$

The log–log regression against the largest Laplacian eigenvalue gives

$$\text{slope} = -2.3870, \qquad R^2 = 0.5392.$$

Figure 4 visualizes the spectral-scaling diagnostic. The observed negative fitted slope and moderate coefficient of determination do not support a positive unit-slope scaling law for the classical-curvature quantity.

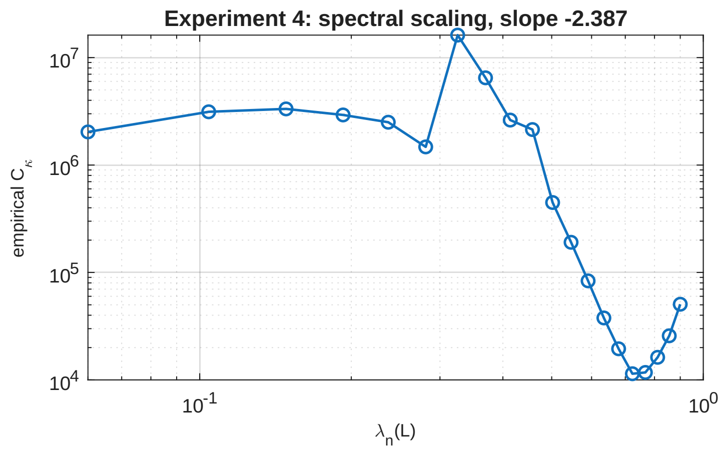

Figure 4. Spectral-scaling diagnostic in Experiment 4. The empirical classical-curvature quantity $C_{\widehat{\kappa}}$ is plotted against the largest graph-Laplacian eigenvalue $\lambda_n(L)$. The observed behavior does not support a positive unit-slope spectral-curvature scaling law.

Hence, the experiment does not support a relation of the form

$$\widehat{C}_\kappa \propto \lambda_n(L)$$

with positive unit slope.

Across the same sweep, the fitted classical-curvature exponents satisfy

$$-0.8350 \leq \widehat{\mu}_\kappa \leq 0.8156.$$

The large variation, including negative values, shows that no architecture-independent classical-curvature decay exponent is supported by this experiment.

Accordingly, Experiment 4 is retained as a diagnostic demonstrating that a positive unit-slope spectral-curvature scaling law is not supported by the simulated family. The rigorous spectral statement in Theorem 6.2 concerns graph diffusion energy only and does not imply monotone dependence of either κ or $K = \kappa v_e^2$ on $\lambda_n(L)$.

7.6. Experiment 5: parameter Monte Carlo robustness

We perform $N = 500$ independent parameter realizations of the constant-delay, constant-weight numerical subclass. The numerical convergence criterion classifies

$$456/500$$

realizations as convergent, corresponding to

$$\boxed{91.2\%}.$$

For the convergent realizations, the empirical error-norm decay exponent has

$$\text{mean}(\widehat{\mu}_e) = 0.5363, \quad \text{std}(\widehat{\mu}_e) = 0.1588,$$
$$\text{median}(\widehat{\mu}_e) = 0.5230, \quad P_{95}(\widehat{\mu}_e) = 0.8158.$$

Thus norm convergence is robust over a substantial part of the sampled parameter range.

The fitted classical-curvature exponent has

$$\begin{aligned} \operatorname{mean}(\widehat{\mu}_\kappa) &= -0.3544, \quad \operatorname{std}(\widehat{\mu}_\kappa) = 0.2353, \\ \operatorname{median}(\widehat{\mu}_\kappa) &= -0.2996, \quad P_{95}(\widehat{\mu}_\kappa) = -0.0870. \end{aligned}$$

The predominantly negative values are consistent with the distinction proved in Theorem 5.1: Exponential norm convergence does not imply decay of classical curvature.

The finite-horizon continuous accumulated-curvature diagnostic

$$\Sigma_{\text{cont}} := \int_0^{50} \kappa(t) v_e(t)\, dt$$

has

$$\begin{aligned} \operatorname{mean}(\Sigma_{\text{cont}}) &= 1.8335, \quad \operatorname{std}(\Sigma_{\text{cont}}) = 1.0563, \\ \operatorname{median}(\Sigma_{\text{cont}}) &= 1.6420, \quad P_{95}(\Sigma_{\text{cont}}) = 3.3831. \end{aligned}$$

These are descriptive finite-horizon quantities only.

The controlled analytical modal diagnostics give

$$\begin{aligned} \operatorname{mean}(A_{\text{near}}) &= 0.7452, \quad \operatorname{std}(A_{\text{near}}) = 0.2447, \\ \operatorname{median}(A_{\text{near}}) &= 0.6968, \quad P_{95}(A_{\text{near}}) = 1.2110, \end{aligned}$$

and

$$\begin{aligned} \operatorname{mean}(A_{\text{det}}) &= 0.5809, \quad \operatorname{std}(A_{\text{det}}) = 0.1456, \\ \operatorname{median}(A_{\text{det}}) &= 0.5591, \quad P_{95}(A_{\text{det}}) = 0.8532. \end{aligned}$$

These quantities are analytical rate-matching diagnostics computed from the sampled decay rates; they are not full PDE simulations for all 500 realizations.

The descriptive statistics obtained from the 456 convergent realizations are summarized in Table 3. The positive values of $\widehat{\mu}_e$ confirm robust error-norm convergence over the sampled parameter ranges, whereas the predominantly negative values of $\widehat{\mu}_\kappa$ show that classical-curvature decay is not supported. Moreover, the larger values of A_{near} relative to A_{det} indicate a stronger transient response in the near-matching regime.

Table 3. Parameter Monte Carlo summary ($N = 500$; 456 convergent realizations, 91.2%).

Quantity	Mean	Std	Median	95th percentile
$\widehat{\mu}_e$	0.5363	0.1588	0.5230	0.8158
$\widehat{\mu}_\kappa$	-0.3544	0.2353	-0.2996	-0.0870
Σ_{cont}	1.8335	1.0563	1.6420	3.3831
A_{near}	0.7452	0.2447	0.6968	1.2110
A_{det}	0.5809	0.1456	0.5591	0.8532

7.7. Experiment 6: network topology sensitivity

Topology-generation protocol. The topology-sensitivity experiment is performed with $n = 20$ and 100 attempted realizations for each graph class. The ring graph has degree $k = 4$, with each node connected to two neighbors on either side. The small-world graph is initialized from the same degree-4 ring, after which the forward ring edges are rewired independently with probability

$$p_{\mathrm{sw}} = 0.10,$$

while preserving an undirected symmetric adjacency matrix and excluding self-loops. For the Erdős–Rényi graph, the edge probability is chosen as

$$p_{\mathrm{er}} = \frac{k}{n-1} = \frac{4}{19},$$

so that the expected degree before isolated-vertex correction is matched to the ring degree. Any isolated vertex is connected by one additional random edge.

For every existing undirected edge, a symmetric random weight is assigned according to

$$w_{ij} = w_{\mathrm{topo}}(0.5 + 0.5U_{ij}), \qquad U_{ij} \sim \mathrm{Unif}(0,1), \qquad w_{\mathrm{topo}} = 0.10.$$

Hence the nonzero weights lie in the interval $[0.05, 0.10)$. No spectral rescaling is applied to impose or equalize a prescribed value of $\lambda_n(L)$. Instead, after each weighted graph is generated, the Laplacian

$$L = D - W$$

is formed and $\lambda_n(L)$ is computed directly as its largest eigenvalue. Thus, the reported values of $\lambda_n(L)$ are measured properties of the generated weighted graphs rather than imposed spectral targets. Disconnected graphs and realizations that fail the contraction screen are discarded before integration; realizations that subsequently fail the numerical convergence criterion are also excluded from the reported valid sample. Topology sensitivity is tested separately with $n = 20$, rather than with the three-dimensional baseline system. This is important because a three-node ring is already the complete graph and therefore does not provide a meaningful ring-versus-random topology comparison.

The numerical results are

Topology	Valid	mean $\lambda_n(L)$	mean $\widehat{\mu}_\kappa$	mean Σ_{cont}
Ring	100/100	0.5110	−0.4852	1.5196
Small-world	100/100	0.5660	−0.5187	1.5655
Erdős–Rényi	97/100	0.7029	−0.5065	1.7599

For the fitted classical-curvature exponent, the Kruskal–Wallis test gives

$$p_{\mu_\kappa} = 0.0332048.$$

Thus the null hypothesis of identical group distributions is rejected at the 5% level. We therefore make no topology-independence claim for $\widehat{\mu}_\kappa$.

For accumulated curvature,

$$p_\Sigma = 8.98017 \times 10^{-14},$$

showing a highly significant topology effect in this simulated family. Among the three sampled topology classes, the Erdős–Rényi ensemble has the largest mean accumulated-curvature value.

These are empirical finite-horizon topology-sensitivity results. They do not contradict Theorem 6.2, which bounds graph disagreement energy and does not assert topology-independence of classical curvature or accumulated curvature.

Remark 7.1 (Interpretation of the robustness experiments)**.** The numerical experiments support three conclusions. First, norm convergence is robust in the parameter Monte Carlo study, with 91.2% of realizations passing the convergence screen. Second, classical curvature does not generically decay even among convergent runs. Third, the $n = 20$ topology study detects statistically significant differences in both $\widehat{\mu}_\kappa$ and Σ_{cont}. These observations are reported as empirical results and are not promoted to spectral-curvature theorems.

8. Conclusions and discussion

8.1. Summary

The main conclusion is a separation principle between norm stability, weighted geometric stabilization, and classical Frenet diagnostics. Exponential convergence of the error norm does not imply exponential decay of the classical curvature. Theorem 5.1 instead controls

$$\mathcal{K}(t) = \kappa(t)v_e(t)^2 = \|P_{T(t)^\perp}\ddot{e}(t)\|,$$

which inherits the acceleration decay assumed in (A9) without requiring a positive lower bound on the speed. Experiment 1 is consistent with this distinction: the weighted-curvature fit gives $\widehat{\mu}_{\mathcal{K}} = 1.0478$ with $R^2 = 0.9914$, whereas the classical-curvature fit gives only $\widehat{\mu}_\kappa = 0.0189$ with $R^2 = 0.0372$.

The PDE conclusions are likewise narrower than in the original formulation. Theorem 5.4 treats multiplicative jumps as contractive operators on the reaction–diffusion field; they do not act as additive wave sources. Proposition 5.6 describes a periodic modal rate-matching transient. The difference quotient has a removable limit when $\rho_m \to \mu$, namely, $\theta e^{-\mu\theta}$, so there is no singular resonance. With the correct three-dimensional torsion formula, the computation gives $\bar{\omega}_g = 23.335979$ from 280 valid samples. The corresponding controlled experiment yields a near/detuned numerical peak ratio 1.2553 and a near-matching peak time 1.9600, compared with the limiting characteristic time $1/\widehat{\mu}_e = 1.9807$.

The spectral theorem concerns a different object:

$$\mathcal{E}(t) = \tfrac{1}{2}e(t)^\top L(t)e(t).$$

It provides an exponential upper envelope proportional to $\bar{\lambda}_n e^{-2\mu(t-t_0)}$ but does not imply a monotone spectral law for classical or weighted curvature. Experiment 4 reinforces this distinction: the fitted log–log slope for the classical-curvature prefactor is -2.3870 with $R^2 = 0.5392$ and therefore does not support a positive unit-slope relation.

In the parameter Monte Carlo study, 456/500 realizations pass the numerical convergence criterion, while the fitted classical-curvature exponent is predominantly negative among those convergent runs. In the separate $n = 20$ topology study, the Kruskal–Wallis tests give $p_{\mu_\kappa} = 0.0332048$ and $p_\Sigma = 8.98017 \times 10^{-14}$. Thus the simulations do not support topology independence of these geometric diagnostics.

8.2. *Relation to prior work*

The present framework complements Lyapunov–Gronwall stability analysis rather than replacing it. The norm estimate inherited from the underlying impulsive delayed CGNN theory supplies the dynamical stability statement; the geometric analysis identifies which derived quantities remain controlled when the trajectory speed tends to zero. The graph-energy result is a spectral consequence of the Laplacian quadratic form applied to the exponentially decaying error, whereas the periodic PDE construction provides a separate controlled modal diagnostic. Keeping these levels distinct prevents norm-stability, Frenet-geometry, and spectral-PDE conclusions from being conflated.

8.3. *Limitations and future work*

Several limitations are essential. First, the weighted-curvature theorem requires the higher-order acceleration estimate in (A9); exponential decay of $\|e(t)\|$ alone is insufficient. Second, scalar torsion and the Frenet frequency diagnostic used here are three-dimensional and are defined only at regular non-inflection points. Near $\dot{e} \times \ddot{e} = 0$, torsion is ill-conditioned, so the numerical procedure explicitly filters non-regular samples. For higher-dimensional state spaces, a Bishop or other moving-frame formulation is preferable.

Third, the Dirichlet H_0^1 PDE estimate and the periodic modal rate-matching experiment serve different purposes and should not be identified as the same boundary-value problem. Fourth, the Monte Carlo and topology results are finite-horizon empirical diagnostics; they do not establish universal probability statements or topology laws. Finally, the present rate-matching experiment uses a deliberately chosen periodic length and an adaptive diffusion coefficient. Future work should test fixed physical domains, independently specified PDE parameters, higher-dimensional moving frames, stochastic perturbations, and data-driven estimation of regular geometric diagnostics.

8.4. *Broader interpretation*

The rigorous geometric statement is the decay of the normal acceleration magnitude $\mathcal{K}$, not the flattening of classical curvature itself. The rigorous graph statement is the decay of the Laplacian disagreement-energy envelope, not the topology independence of curvature. The PDE calculation identifies a finite modal rate-matching transient, not an unbounded resonance mechanism.

These distinctions may be useful when delayed impulsive network models are employed as reduced descriptions of coupled physical, biological, or engineering systems. Application-specific claims, however, require an explicit model reduction linking the state variables, graph, forcing, and PDE parameters to measurable quantities. The present results should therefore be viewed as a mathematical framework for such studies rather than as direct validation for a particular physical or biological system.

Author contributions

Münevver Tuz: Conceptualisation, geometric framework, theorem proofs, numerical experiments; Gülden Altay Suroğlu: Literature integration, writing, editing. Both authors approved the final manuscript.

Use of Generative-AI tools declaration

The authors made limited use of AI solely for English-language editing and improving the readability of the manuscript. All resulting suggestions were carefully reviewed and revised by the authors, who take full responsibility for the final content.

Funding

This work was supported by the Fırat University Scientific Research Projects (FÜBAP), grant FF.25.44.

Conflict of interest

The authors declare no conflicts of interest.

References

1. J. J. Hopfield, Neural networks and physical systems with emergent collective computational abilities, *Proc. Natl. Acad. Sci. USA*, **79** (1982), 2554–2558. https://doi.org/10.1073/pnas.79.8.2554
2. B. Kosko, Bidirectional associative memories, *IEEE Trans. Syst. Man Cybern.*, **18** (1988), 49–60. https://doi.org/10.1109/21.87054
3. T. Chen, Global exponential stability of delayed Hopfield-type neural networks, *Neural Networks*, **14** (2001), 977–980. https://doi.org/10.1016/s0893-6080(01)00059-4
4. M. A. Cohen, S. Grossberg, Absolute stability of global pattern formation and parallel memory storage by competitive neural networks, *IEEE Trans. Syst. Man Cybern.*, **SMC-13** (1983), 815–826. https://doi.org/10.1109/TSMC.1983.6313075
5. Z. Liu, A. Chen, J. Cao, L. Huang, Existence and global exponential stability of periodic solution for BAM neural networks with periodic coefficients and time-varying delays, *IEEE Trans. Circuits Syst. I*, **50** (2003), 1162–1173. https://doi.org/10.1109/TCSI.2003.816306
6. J. Liang, J. Cao, Exponential stability of continuous-time and discrete-time bidirectional associative memory networks with delays, *Chaos Soliton. Fract.*, **22** (2004), 773–785. https://doi.org/10.1016/j.chaos.2004.03.004
7. S. Arik, Global asymptotic stability analysis of bidirectional associative memory neural networks with time delays, *IEEE Trans. Neural Networks*, **16** (2005), 580–586. https://doi.org/10.1109/TNN.2005.844910
8. A. Chen, L. Huang, J. Cao Existence and stability of almost periodic solutions for BAM neural networks with delays, *Appl. Math. Comput.*, **137** (2003), 177–193. https://doi.org/10.1016/S0096-3003(02)00095-4

9. C. Zhang, F. Yang, W. Li, D. Wu, J. Yang, Global exponential stability of BAM type Cohen–Grossberg neural networks with delays and impulsive, *2008 IEEE International Conference on Automation and Logistics*, 2008, 3055–3059. https://doi.org/10.1109/ICAL.2008.4636703

10. F. Yang, C. Zhang, D. Wu, Global stability of impulsive BAM type Cohen–Grossberg neural networks with delays, *Appl. Math. Comput.*, **186** (2007), 932–940. https://doi.org/10.1016/j.amc.2006.08.016

11. W. Ding, L. Wang, 2^N almost periodic attractors for Cohen–Grossberg-type BAM neural networks with variable coefficients and distributed delays, *J. Math. Anal. Appl.*, **373** (2011), 322–342. https://doi.org/10.1016/j.jmaa.2010.06.055

12. M. Tuz, G. A. Suroğlu, New insights into delay-impulsive interactions and stability in almost periodic Cohen–Grossberg neural networks, *Symmetry*, **17** (2025), 2063. https://doi.org/10.3390/sym17122063

13. T. Ivancevic, L. Jain, J. Patttison, A. Hariz, Nonlinear dynamics and chaos methods in neurodynamics and complex data analysis, *Nonlinear Dynam.*, **56** (2009), 23–44. https://doi.org/10.1007/s11071-008-9376-9

14. A. Wan, H. Qiao, J. Peng, M. Wang, Delay-independent criteria for exponential stability of generalised Cohen–Grossberg neural networks with discrete delays, *Phys. Lett. A*, **353** (2006), 151–157. https://doi.org/10.1016/j.physleta.2005.12.085

15. K. Li, Delay-dependent exponential stability analysis for impulsive BAM neural networks with time-varying delays, *Comput. Math. Appl.*, **56** (2008), 2088–2099. https://doi.org/10.1016/j.camwa.2008.03.038

16. M. Luo, J. Jiao, R. Wang, Impulsive control of a nonlinear dynamical network and its application to biological networks, *J. Biol. Phys.*, **45** (2019), 31–44. https://doi.org/10.1007/s10867-018-9513-8

17. M. Akhmet, M. Tleubergenova, A. Zhamanshin, Z. Nugayeva, *Artificial neural networks: Alpha unpredictability and chaotic dynamics*, Springer Cham, 2025. https://doi.org/10.1007/978-3-031-68966-6

18. J. Hu, Z. Wang, G. P. Liu, Delay compensation-based state estimation for time-varying complex networks with incomplete observations and dynamical bias, *IEEE Trans. Cybern.*, **52** (2022), 12071–12083. https://doi.org/10.1109/TCYB.2020.3043283

19. M. Akhmet, M. Tleubergenova, R. Seilova, Z. Nugayeva, Symmetrical impulsive inertial neural networks with unpredictable and Poisson-stable oscillations, *Symmetry*, **15** (2023), 1812. https://doi.org/10.3390/sym15101812

20. H. Bohr, *Almost periodic functions*, Chelsea Publishing, New York, 1947.

21. A. M. Fink, *Almost periodic differential equations*, Berlin: Springer, 1974. https://doi.org/10.1007/bfb0070324

22. G. T. Stamov, *Almost periodic solutions of impulsive differential equations*, Berlin: Springer, 2012. https://doi.org/10.1007/978-3-642-27546-3

23. S. Ponomarev, J. F. Couchouron, M. I. Kamenskii, Almost periodic solutions of evolution equations, *Topol. Methods Nonlinear Anal.*, **50** (2017), 65–87. https://doi.org/10.12775/tmna.2017.012

24. Y. Liu, Z. You, L. Cao, On the almost periodic solution of generalised Hopfield neural networks with time-varying delays, *Neurocomputing*, **69** (2006), 1760–1767. https://doi.org/10.1016/j.neucom.2005.12.117

25. H. Xiang, J. Wang, J. Cao, Almost periodic solution to Cohen–Grossberg-type BAM networks with distributed delays, *Neurocomputing*, **72** (2009), 3751–3759. https://doi.org/10.1016/j.neucom.2009.05.014

26. L. Gao, Z. Liu, S. Yang, The input-to-state stability in probability for constrained delay systems with stochastic delayed impulses, *IEEE Trans. Autom. Sci. Eng.*, **22** (2025), 9205–9217. https://doi.org/10.1109/tase.2024.3502656

27. K. Li, H. Zeng, Stability in impulsive Cohen–Grossberg-type BAM neural networks with time-varying delays: a general analysis, *Math. Comput. Simul.*, **80** (2010), 2329–2349. https://doi.org/10.1016/j.matcom.2010.05.012

28. M. Bohner, G. T. Stamov, I. M. Stamova, Almost periodic solutions of Cohen–Grossberg neural networks with time-varying delay and variable impulsive perturbations, *Commun. Nonlinear Sci. Numer. Simul.*, **80** (2020), 104952. https://doi.org/10.1016/j.cnsns.2019.104952

29. A. A. Agrachev, Y. L. Sachkov, *Control theory from the geometric viewpoint*, Berlin: Springer, 2004. https://doi.org/10.1007/978-3-662-06404-7

30. R. L. Bishop, There is more than one way to frame a curve, *Amer. Math. Monthly*, **82** (1975), 246–251. https://doi.org/10.1080/00029890.1975.11993807

31. M. P. do Carmo, *Differential geometry of curves and surfaces*, Prentice-Hall, Englewood Cliffs, 1976.

32. J. P. Hespanha, A. S. Morse, Stability of switched systems with average dwell-time, *Proceedings of the 38th IEEE Conference on Decision and Control (Cat. No.99CH36304)*, Phoenix, AZ, 1999, 2655–2660. https://doi.org/10.1109/cdc.1999.831330

33. K. Gopalsamy, *Stability and oscillations in delay differential equations of population dynamics*, Dordrecht: Kluwer Academic Publishers, 1992. https://doi.org/10.1007/978-94-015-7920-9

34. F. A. Rihan, *Delay differential equations and their applications in biology*, Forum for Interdisciplinary Mathematics, Springer, 2021. https://doi.org/10.1007/978-981-16-0626-7

35. W. Zhang, J. Huang, Stability analysis of stochastic delayed differential systems with state-dependent-delay impulses: application of neural networks, *Cogn. Comput.*, **14** (2022), 805–813. https://doi.org/10.1007/s12559-021-09967-x

36. W. Yang, W. Yu, J. Cao, F. E. Alsaadi, T. Hayat, Global exponential stability and lag synchronization for delayed memristive fuzzy Cohen–Grossberg BAM neural networks with impulses, *Neural Networks*, **98** (2018), 122–153. https://doi.org/10.1016/j.neunet.2017.11.001

37. M. Akhmet, E. Yılmaz, *Neural networks with discontinuous/impact activations*, Nonlinear Systems and Complexity, Vol. 9, New York: Springer, 2014. https://doi.org/10.1007/978-1-4614-8566-7

38. F. H. Clarke, *Optimization and nonsmooth analysis*, Philadelphia: SIAM, 1990. https://doi.org/10.1137/1.9781611971309

39. P. Li, R. Gao, C. Xu, Y. Li, A. Akgül, D. Baleanu, Dynamics exploration for a fractional-order delayed zooplankton–phytoplankton system, *Chaos Soliton. Fract.*, **166** (2023), 112975. https://doi.org/10.1016/j.chaos.2022.112975

40. F. R. K. Chung, *Spectral graph theory*, CBMS Regional Conference Series in Mathematics, Vol. 92, Providence: AMS, 1997. https://doi.org/10.1090/cbms/092

41. Q. Ma, S. Xu, Intentional delay can benefit consensus of second-order multi-agent systems, *Automatica*, **147** (2023), 110750. https://doi.org/10.1016/j.automatica.2022.110750